Interfacial reactions of titanium/gold ohmic contacts with Sn-doped β-Ga_2O_3

Cite as: APL Mater. 7, 022524 (2019); doi: 10.1063/1.5054624
Submitted: 31 August 2018 • Accepted: 10 January 2019 •
Published Online: 1 February 2019

Ming-Hsun Lee[1] and Rebecca L. Peterson[2]

AFFILIATIONS

[1]Materials Science and Engineering Department, University of Michigan, Ann Arbor, Michigan 48109, USA
[2]Electrical Engineering and Computer Science Department, University of Michigan, Ann Arbor, Michigan 48109, USA

ABSTRACT

Here we investigated interfacial reactions and interdiffusion of titanium/gold ohmic contacts with a tin-doped single-crystal β-Ga_2O_3 (010) substrate. After annealing at 470 °C for 1 min in N_2 to form an ohmic contact, we studied the interface via scanning transmission electron microscopy and transmission electron microscopy with energy dispersive X-ray spectroscopy as well as electron energy loss spectroscopy. At the interface, annealing causes Ti to diffuse and oxidize, reducing Ga_2O_3 at the interface. This forms a defective β-Ga_2O_3 layer of 3-5 nm that has a relatively high Ti concentration. Above this is a 3-5 nm layer of Ti-TiO_x that is partially lattice matched to the β-Ga_2O_3 substrate. The thermodynamic favorability of these redox reactions was explained by calculating Gibbs free energies of the reactions. In addition, the anneal causes interdiffusion of Ti and Au, until Au is in contact with the thin Ti-TiO_x layer. A layer of Ti-rich nanocrystals, around 5 nm in diameter, is formed within the Au-Ti intermixed matrix, about 3 nm above the Ti-TiO_x layer. Based on these observations, the ohmic properties are tentatively attributed to the interdiffusion of Ti and Au and the resulting thin Ti-TiO_x layer, which helps band alignment. In addition, lattice matching of the defective Ga_2O_3 and Ti-TiO_x layers to β-Ga_2O_3 facilitates the transport of carriers. A physical understanding of Ti/Au metallization can provide insights into future materials selection for thermally stable contacts in β-Ga_2O_3 power devices.

β-Ga_2O_3, a next-generation wide bandgap (WBG) semiconductor, has recently attracted worldwide attention owing to its enormous potential for high power electronics. The reported bandgap of β-Ga_2O_3 ranges from 4.6 to 4.9 eV, significantly exceeding that of other WBG semiconductors such as 4H-SiC (E_g = 3.2 eV) and GaN (E_g = 3.4 eV). The large bandgap indicates that beta-phase gallium oxide should be able to withstand a larger electric field before avalanche multiplication compared to SiC and GaN; this has already been observed experimentally.[1–3] A large critical e-field enables power devices with high breakdown voltages, V_{br}, and low specific on-resistance, $R_{on,sp}$. Accordingly, Baliga's figure of merit (BFOM) is expected to be over 34 000 MW cm^{-2}, which is more than ten times that of 4H-SiC and four times that of GaN.[4–7] In addition, bulk single crystal β-Ga_2O_3 can be prepared by a number of techniques, including float zone growth,[8] Czochralski growth,[9] and edge-defined film-fed growth,[10] and is commercially available. Moreover, β-Ga_2O_3 can be doped extrinsically by Sn, Si, and Ge across a wide range from 10^{16} to 10^{19} cm^{-3}. All of these traits give β-Ga_2O_3 a significant advantage over other WBG semiconductors. Sn-doped β-Ga_2O_3, the subject of the current study, has been investigated and used in various electronic devices.[5,6] Recently, β-Ga_2O_3 metal-oxide-semiconductor field effect transistors (MOSFETs) with V_{br} > 1.85 kV and Schottky barrier diodes (SBDs) with V_{br} > 1 kV have been demonstrated.[2,3,11]

Low ohmic contact resistance with thermal stability is required for power devices in order to minimize power loss and enable operation at elevated temperatures. Nearly all of the Ga_2O_3 thin film ohmic metallization schemes shown to date use a titanium interfacial layer with additional capping layers such as Ti/Au or Ti/Al/Ni/Au to lower metal film resistance and reduce surface oxidation.[6] Post-metallization anneals at 400 °C-500 °C in a reducing environment, typically nitrogen, are widely used[1,12–16] to form an ohmic contact to Sn-doped β-Ga_2O_3. The lowest specific contact resistance, ρ_c, achieved on Sn-doped β-Ga_2O_3 was[15] 2.1 ± 1.4 × 10^{-5} Ω cm^2,

while 4.6×10^{-6} to 8.1×10^{-6} Ω cm^2 was achieved[12,17] on Si-ion implanted β-Ga_2O_3. Higashiwaki *et al.*, observed a defective Ga_2O_3 layer and a reacted Ti/Ga_2O_3 layer at the annealed interface of Ti/Au and Si-implanted β-Ga_2O_3.[12] However, the interfacial reactions that contribute to ohmic behavior are still not clear. Here we investigated Ti/Au contact metallization on Sn-doped β-Ga_2O_3 with scanning transmission electron microscopy/transmission electron microscopy (STEM/TEM). We demonstrate that even after a very brief (1-min) 470 °C anneal, Au and Ti suffer from significant diffusion. After annealing, the highest Ti concentration is found in a thin (~5 nm) layer of Ti-TiO_x near the interface. A portion of this Ti-TiO_x layer is lattice matched with β-Ga_2O_3. The remainder of the Ti has diffused into the adjacent Au and Ga_2O_3 layers. Below the Ti-TiO_x layer, there is a 3-5 nm defective β-Ga_2O_3 layer that has significant Ti incorporation while preserving the monoclinic structure. Above the Ti-TiO_x layer, intermixed Au-Ti exists, with a layer of Ti-rich nanocrystallites embedded within it. Via chemical mapping, electron microscopy imaging, and selected area diffraction patterns, we confirm the multilayer micro-structure and propose possible reasons for ohmic contact formation at the Ti/Au–β-Ga_2O_3 interface.

10 × 15 mm^2 Sn-doped β-Ga_2O_3 (010) substrates, with a chemical mechanical polished surface and ~500-μm thickness, *t*, were purchased from Tamura Corp. The donor concentration, N_D, was reported by Tamura to be ~2.6×10^{18} cm^{-3}, based on C-V measurements. Upon receipt, the substrates were diced into 5 × 5 mm^2 square pieces and solvent cleaned with acetone, isopropyl alcohol, and methanol in a 40 °C ultrasonic tank for 10 min each. Next, circular transmission line model (CTLM) structures [Fig. 1(a), inset] were made using standard photo-lithography followed by an O_2 plasma descum at 40 °C for 80 s (YES Plasma Stripper). Using e-beam, 20 nm of Ti and 80 nm of Au were evaporated (EnerJet Evaporator) and patterned by lift-off. Finally, the pieces were subjected to rapid thermal annealing (JetFirst-150 RTP) for 1 min at 470 °C in N_2 to obtain an ohmic contact, following the recipe published by Higashiwaki *et al.* in 2013.[12] Reactive ion etching (RIE) and Si ion-implantation have been reported as effective ways to suppress contact resistance and improve ohmic performance.[12] In order to minimize the number of factors that might influence interfacial reactions, we did not use RIE or ion implant for this study. Nevertheless, we were able to obtain ohmic characteristics on Sn-doped β-Ga_2O_3 substrates.

For electrical measurements, we employed Kelvin probing (four probe) measurements using a Keysight B1505A Power Device Analyzer and Cascade MicroTech Tesla probe station. Two of the probes were landed on the inside CTLM contact pad, while the other two were landed on the outside contact. This configuration eliminates parasitic contribution from the probes used to contact the metal pads. Voltage was applied from −50 mV to +50 mV with a 1 mV step while measuring current. Since the devices did not show noticeable hysteresis when measuring with a double sweep (forward-reverse), we performed all the measurements described here using a single, forward sweep.

To investigate interface reactions, transmission electron microscopy (TEM) samples were prepared with a β-Ga_2O_3 (001) surface plane via focused ion beam (FIB)-assisted lift-out using a FEI Nova 200 Nanolab and a FEI Helios 650 Nanolab. Prior to FIB, the tops of the samples were capped with 1 μm carbon and 1 μm platinum to prevent FIB damage during lift-out. After lift-out, the samples were attached to a Cu TEM grid followed by thinning. Because the β-Ga_2O_3 substrate is comparatively harder than the capping layers, a large amount of overtilt (±8° normal to the FIB gun) was used during the final thinning. The final thickness was around 106 nm based on electron energy loss spectroscopy (EELS) measurements. After preparation, scanning transmission electron microscopy (STEM) imaging, energy-dispersive x-ray spectroscopy (EDX), and EELS analyses were performed on a JEOL 2100F Analytical Electron Microscope (AEM). TEM images were taken using JEOL 2010F AEM, and fast Fourier transform (FFT) patterns of selected area electron diffraction (SAED) were obtained from a Gatan Digital Micrograph.

Figure 1(a) shows the current-voltage (I-V) characteristics of our Sn-doped β-Ga_2O_3 CTLM structures with contact spacing, *d*, equal to 25, 35, 40, 45, and 50 μm. Linear I-V curves were observed, indicating ohmic contacts. The total resistances extracted are within the range of 2.26 Ω–3.21 Ω [Fig. 1(b)].

According to CTLM theory,[17,18] the total resistance measured, R_T (Ω), should obey

$$R_T = \frac{R''_{sh}}{2\pi}\frac{L_T}{r_i}\frac{I_0(r_i/L_T)}{I_1(r_i/L_T)} + \frac{R_{sh}}{2\pi}\ln\left(\frac{r_i+d}{r_i}\right) + \frac{R''_{sh}}{2\pi}\frac{L_T}{(r_i+d)}\frac{K_0((r_i+d)/L_T)}{K_1((r_i+d)/L_T)}, \quad (1)$$

where the first, second, and third terms indicate the inner contact resistance, R_{inner}, the semiconductor resistance of the gap, R_{gap}, and the outer contact resistance, R_{outer}, respectively. Here r_i is the inner radius of the CTLM structures, which is 300 μm in our devices, and *d* is the gap spacing between the inner and the outer contact pads, as shown in the inset of Fig. 1(a). I_0 and I_1 are the zeroth and first order modified Bessel functions of the first kind, and K_0 and K_1 are the zeroth and first order modified Bessel functions of the second kind. $L_T = (\rho_c/R''_{sh})^{0.5}$ is the transfer length, where ρ_c is the specific contact resistance and R_{sh} and R''_{sh} are the Ga_2O_3 substrate sheet resistance in units of Ω per square (Ω/□) in the gap and under the metal, respectively. Using centimeter-scale van der Pauw structures, we measure the bulk sheet resistance of our Sn-doped β-Ga_2O_3 substrate to be 0.6 Ω/□, which corresponds to a bulk substrate resistivity of $\rho = R_{sh} \cdot t = (q\mu_e N_D)^{-1}$ = 0.03 Ω cm.

The use of the bulk R_{sh} value in Eq. (1) requires[18] that the thickness of the semiconductor layer, *t*, be much less than the electrode spacing, *d*, i.e., $t \ll d$. For our CTLM structures, this criterion is not valid: *d*, which ranges from 20 to 50 μm, is much smaller than the thickness, which is 500 μm. In this case, conduction in the semiconductor does not occur throughout the whole thickness. Instead, current flows predominantly in a top layer of the semiconductor, near the surface, increasing

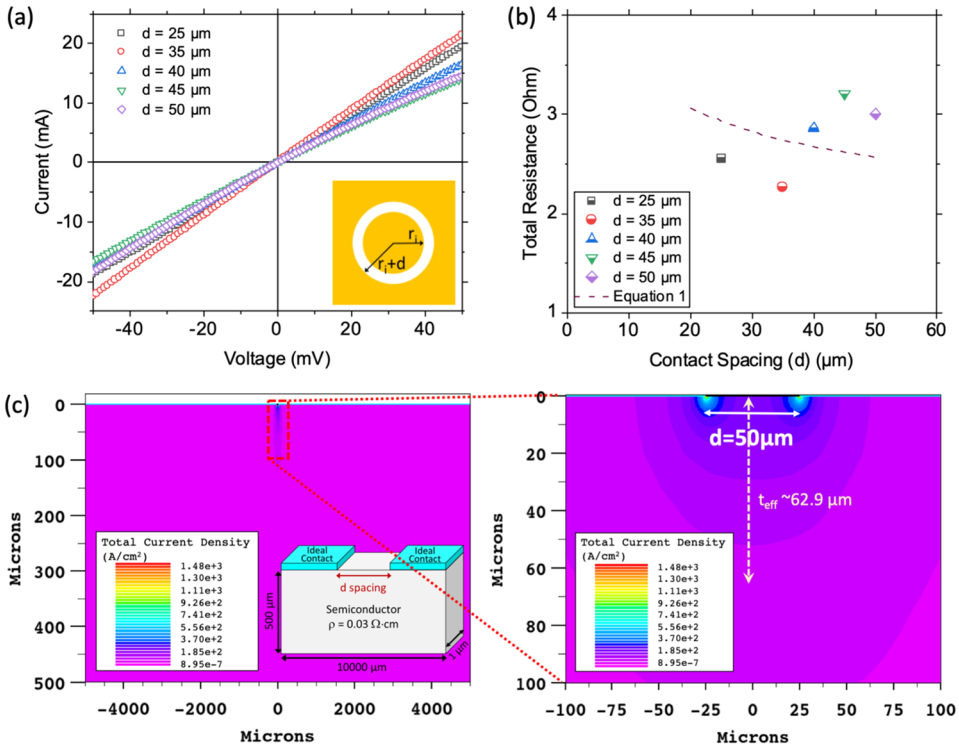

FIG. 1. (a) Current-voltage characteristics of CTLM devices on Sn-doped β-Ga_2O_3 samples. The inset shows a schematic illustration of the CTLM structures with an inner radius, r_i, of 300 μm and contact spacing, d, which varies from 25 μm to 50 μm. (b) Plot of resistance versus contact spacing, d, for CTLM devices. Measured data are indicated with symbols; the dashed line represents values calculated using Eq. (1), as described in the text, with $\rho_c = 5 \times 10^{-3}$ Ω cm^2. (c) Two-dimensional plot of total current density from Silvaco simulation with d = 50 μm. Conduction in the semiconductor is concentrated at the surface. The effective conduction thickness, t_{eff}, is calculated to be 62.9 μm. The inset shows the simulated structure. (d) Table of effective thickness, effective semiconductor sheet resistance, and CTLM resistance components as a function of d. Resistance values are calculated with $\rho_c = 5 \times 10^{-3}$ Ω cm^2, and the total resistance values are plotted in the dashed line of (b).

(d) **CLTM structure resistance as a function of spacing, *d***

d	(μm)	20	30	40	50	500	3800
t_{eff}	(μm)	31.1	42.7	53.2	62.9	267	450
R'_{sh}	(Ω/□)	9.65	7.03	5.65	4.78	1.12	0.67
R_{inner}	(Ω)	2.13	2.03	1.98	1.95	-	-
R_{gap}	(Ω)	0.10	0.11	0.11	0.12	-	-
R_{outer}	(Ω)	0.83	0.67	0.57	0.50	-	-
R_{total}	(Ω)	3.06	2.81	2.67	2.57	-	-

the effective sheet resistance of the semiconductor. In order to quantify the effective thickness of the conduction layer, we employ Silvaco Atlas numerical simulations to calculate the resistance, R_{sim}, between two ideal contacts to a semiconductor in the case where $d \ll t$ [Fig. 1(c)]. We then calculate the effective semiconductor thickness, t_{eff}, which contributes to current flow as

$$t_{eff} = \frac{\rho}{R_{sim}} \frac{d}{w}, \tag{2}$$

where ρ is the resistivity of the semiconductor, 0.03 Ω cm, as above, d is the spacing between the contacts, and the out-of-plane width, w, is 1 μm, as specified in the Silvaco simulation. Hence, an effective semiconductor sheet resistance, R'_{sh}, can be expressed as

$$R'_{sh} = \frac{\rho}{t_{eff}} = \frac{R_{sim} w}{d}. \tag{3}$$

The t_{eff} and R'_{sh} values obtained from simulation are given in Fig. 1(d). When the contact gap, d, is small (20–50 μm), the effective thickness is of the same order of magnitude as d. When the contact gap exceeds the thickness, e.g., d = 3800 μm, conduction occurs throughout the majority of the semiconductor thickness and the value of R'_{sh} approaches the bulk R_{sh} value of 0.6 Ω/□.

To numerically evaluate the specific contact resistance, we use R'_{sh} in place of R_{sh} in Eq. (1) and assume that the semiconductor sheet resistance is the same under the metal and within the gap, that is, $R''_{sh} = R'_{sh}$. The best fit to the data, shown in Fig. 1(b), corresponds to $\rho_c = 5 \times 10^{-3}$ Ω cm^2, and the calculated resistance values from Eq. (1) are given in Fig. 1(d). We observe that the semiconductor CTLM gap contributes less than 5% of the total resistance; the majority of the measured resistance comes from the metal-semiconductor contact. We moreover note that the measured and predicted R_T versus d trends are different. This may be due to the fact that Eq. (1) models the outer contact as an annulus,[19] whereas in practice electrical contact to the outer electrode is made through a needle probe at discrete locations.

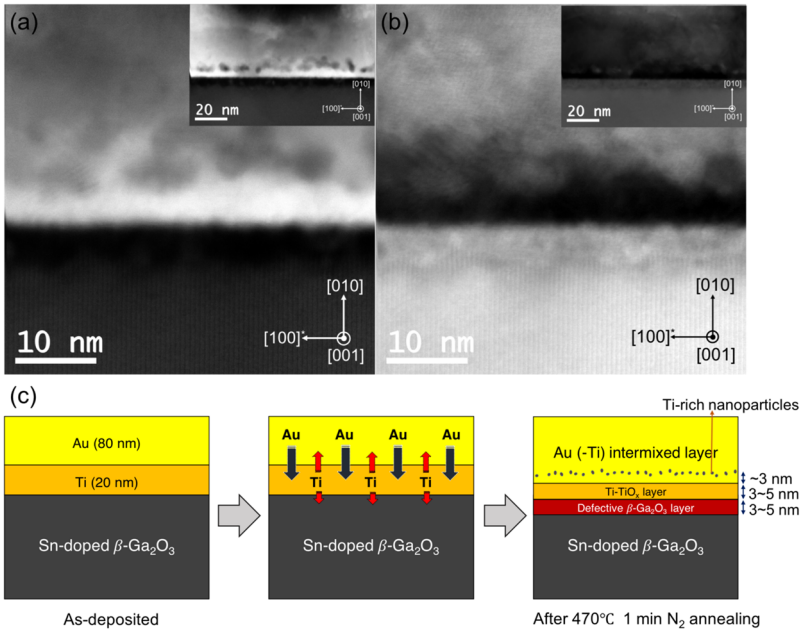

FIG. 2. (a) High-angle annular dark field (HAADF) and (b) bright field (BF) scanning transmission electron microscopy (STEM) images of Ti/Au metallization on Sn-doped β-Ga_2O_3 after 470 °C 1 min N_2 annealing. Insets are the field of view in low magnification. The images show (from the bottom to top) the β-Ga_2O_3 substrate, a defective β-Ga_2O_3 region, a Ti-TiO_x region, an Au rich layer, Ti- or TiO_x-rich nanoparticles, and Au-Ti intermixed layer. (c) Schematic illustrations of the evaluation of the Ti/Au metallization layers on Sn-doped β-Ga_2O_3 following a 1-min 470 °C N_2 anneal.

Thus, the sheet resistance of the metal (20-nm Ti/80-nm Au contact layer yields 0.3 Ω/□) may add a non-trivial series resistance, the value of which can change from measurement to measurement depending on the locations of the probes. In addition, our assumption that the effective Ga_2O_3 sheet resistance under the metal is the same as that in the gap, i.e., $R''_{sh} = R'_{sh}$, where the latter is a function of d, may not be correct. In the future, to enable more accurate measurement of contact resistance, a thinner semiconductor layer (such that $t \ll d$) and thicker metallization should be used. While the ρ_c measured here is higher than that obtained by other groups[15] on Sn-doped Ga_2O_3, nonetheless our Ti/Au contacts exhibit linear I-V (ohmic) behavior and can be used to study the reactions at the interface.

To understand the formation of ohmic contacts, we employed transmission electron microscopy to study the interfacial region. The results from STEM, TEM with FFT, HRTEM, EDX mapping, and EELS mapping are shown in Figs. 2–6, respectively. We discovered that three interfacial layers are formed in the contact region after the brief, 1-min anneal at 470 °C. These three interfacial layers are (from bottom to top) (1) a 3-5 nm defective β-Ga_2O_3 layer, (2) a 3-5 nm Ti-TiO_x layer, and (3) an intermixed Au-Ti layer containing Ti-rich nanocrystalline inclusions. These nanocrystallites are located ~3 nm above the Ti-TiO_x layer. Figure 2(c) shows a schematic illustration of the proposed evolution of the contact interface. We now analyze each of these interfacial layers in turn.

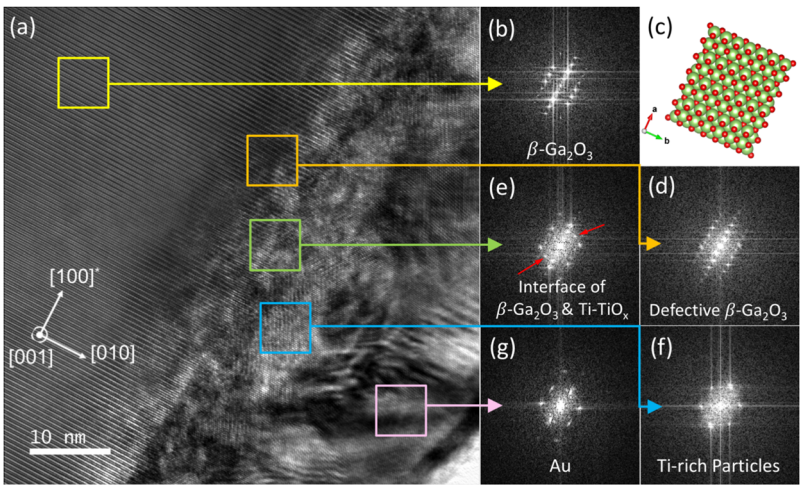

FIG. 3. (a) TEM image of the Ti/β-Ga_2O_3 interface and corresponding FFT diffraction patterns of different regions: (b) β-Ga_2O_3, (d) defective β-Ga_2O_3, (e) Interface of β-Ga_2O_3 & Ti-TiO_x, (f) Ti-rich particles, and (g) Au. In (c), a hard-ball model of β-Ga_2O_3 is shown with the same crystal orientation as the TEM image. The model was generated using VESTA software. The diffraction points highlighted by red arrows in (e) indicate a non-monoclinic structure within the Ti-TiO_x layer.

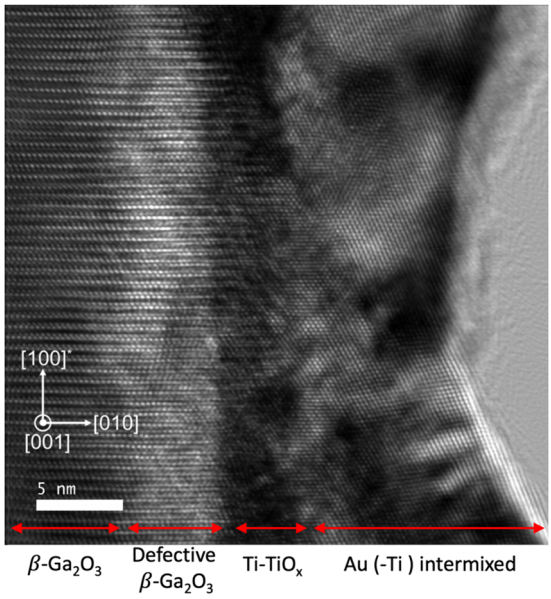

FIG. 4. High resolution TEM image of the Ti/β-Ga_2O_3 interface. Lattice matching above the interface and additional defects below the interface can be seen.

Using STEM, TEM FFT, and HRTEM, we observe a defective β-Ga_2O_3 interfacial layer [Figs. 2(b), 3(d), and 4]. A similar layer was previously observed by Higashiwaki *et al.*[17] for an annealed Ti/Au interface with Si-implanted β-Ga_2O_3. Based on the lattice planes shown in HRTEM (Fig. 4), we observe that the layer largely preserves the monoclinic lattice structure of the β-Ga_2O_3 substrate. Figures 3(b) and 3(d) show FFT diffraction patterns corresponding to the β-Ga_2O_3 bulk crystal and defective β-Ga_2O_3 interfacial layer, respectively. The similarity of the FFT patterns also indicates that the defective β-Ga_2O_3 layer preserves the monoclinic crystal structure. However, within the defective β-Ga_2O_3 region in Figs. 3(a) and 4, some lattice distortions and/or additional defects can be seen. Looking at EDX [Fig. 5(e)] and EELS (Fig. 6) chemical mapping, we note that a non-negligible amount of Ti is incorporated into the defective β-Ga_2O_3 layer. Therefore, we tentatively attribute the formation of this layer to Ti diffusion into the β-Ga_2O_3 substrate. The ionic radii[20] of Ti^{+3}, 67 pm, and Ti^{+4}, 61 pm, are similar to that of Ga^{+3}, 62 pm, which facilitates diffusion. This phenomenon agrees with the observation of Manandhar and Ramana[21] that up to 1.5 at. % Ti can incorporate into β-Ga_2O_3 while preserving the crystal structure of Ga_2O_3. Furthermore, it has been proposed that Ti^{4+} can substitute on octahedral Ga sites, forming a deep donor level 1.6–1.8 eV below the conduction band.[22–24] It is generally agreed[25–29] that oxygen and gallium vacancies do not form shallow donors in β-Ga_2O_3, whereas interstitial hydrogen can lead to shallow donors.[25,26,28] Therefore, stoichiometric defects that could lead to ohmic contact behavior at the interface could include interstitial hydrogen, substitutional silicon, tin, or titanium.

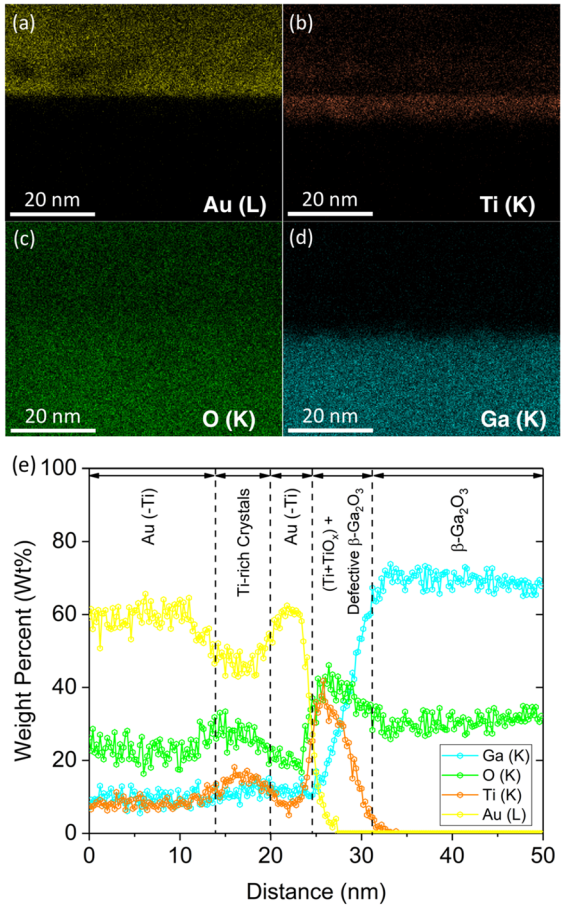

FIG. 5. [(a)–(d)] EDX elemental mapping of four chemical species (Au, Ti, O, and Ga). (e) EDX line scan across the interface. Five distinct layers are observed. From bottom to top, these are β-Ga_2O_3, TiO_x + defective β-Ga_2O_3, intermixed Au-Ti, Ti-rich nanocrystals, and an Au-Ti intermixed capping layer.

On top of the defective β-Ga_2O_3, an ~3-5 nm layer of Ti-TiO_x was observed, as drawn schematically in Fig. 2(c). This layer was observed in EDX [i.e., at a depth of 25-28 nm in Fig. 5(e)] and is confirmed by the overlapping Ti and O (but not Ga) EELS regions in Fig. 6. At the boundary of the Ti-TiO_x region [Fig. 3(e)], the monoclinic diffraction points coexist with other diffraction points, indicating a transition away from the lattice-matched monoclinic interface. Based on HRTEM (Fig. 4), the portion of the Ti-TiO_x layer adjacent to the substrate is lattice matched with β-Ga_2O_3, while the portion farthest away from the Ga_2O_3 substrate may have a different crystal structure.

The driving force for the creation of these two layers can be explained by thermodynamic analysis. One way to predict the thermodynamic favorability of a reaction is by calculating its Gibbs free energy, ΔG_{rxn},

$$\Delta G_{rxn} = \sum \Delta G_f(products) - \sum \Delta G_f(reactants), \qquad (4)$$

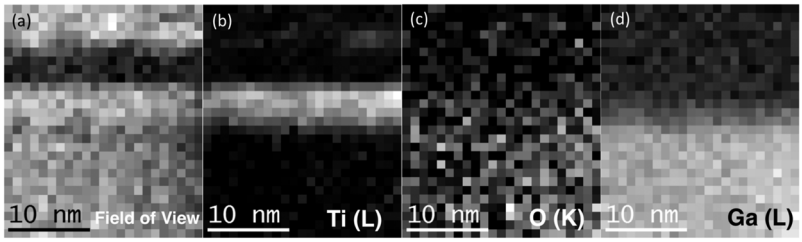

FIG. 6. EELS (a) field of view and mapping in counts of (b) Ti, (c) O, and (d) Ga on a black-white scale, where black is 0% and white is 100%. The distribution of Ti, O, and Ga agrees with that observed by EDX in Fig. 5. We could not resolve Au via EELS because the Au peak position is beyond the measurement range.

$$\Delta G_f = \Delta H_f - T\Delta S, \tag{5}$$

where for a given compound ΔH_f is its enthalpy of formation and ΔS is its entropy difference at temperature, T, in Kelvin, compared with that at absolute zero (0 K). The reaction at the interface of a metal, M, with Ga_2O_3, and its free energy calculation thus can be written as

$$\frac{3x}{y}\mathrm{M(s)} + \mathrm{Ga_2O_3\,(s)} \leftrightarrow 2\mathrm{Ga} + \frac{3}{y}\mathrm{M_xO_y\,(s)}, \tag{6}$$

$$\begin{aligned}\Delta G_{rxn} = &\left[\frac{3}{y}\Delta H_f\left(\mathrm{M_xO_y}\right) + 2\Delta H_f(\mathrm{Ga}) - \frac{3x}{y}\Delta H_f(\mathrm{M}) - \Delta H_f(\mathrm{Ga_2O_3})\right] \\ &- \frac{T}{1000}\times\left[\frac{3}{y}\Delta S\left(\mathrm{M_xO_y}\right) + 2\Delta S(\mathrm{Ga})\right. \\ &\left. - \frac{3x}{y}\Delta S(\mathrm{M}) - \Delta S(\mathrm{Ga_2O_3})\right].\end{aligned} \tag{7}$$

The enthalpy and entropy values at 470 °C (743 K) for the compounds analyzed here are listed in Table I. Based on the free energy calculations performed using Eq. (7), the reactions (8)–(11) for forming TiO_2, Ti_3O_5, Ti_2O_3, and TiO are all more negative in free energy than a metallic Ti/Ga_2O_3 interface. In reactions (8)–(11), elemental Ga, which has a melting point[30] of 302.9 K, may be either liquid or solid, depending on the temperature,

$$1.5\,\mathrm{Ti\,(s)} + \mathrm{Ga_2O_3\,(s)} \leftrightarrow 2\,\mathrm{Ga} + 1.5\,\mathrm{TiO_2\,(s)}, \tag{8}$$

$$1.8\,\mathrm{Ti\,(s)} + \mathrm{Ga_2O_3\,(s)} \leftrightarrow 2\,\mathrm{Ga} + 0.6\,\mathrm{Ti_3O_5\,(s)}, \tag{9}$$

$$2\,\mathrm{Ti\,(s)} + \mathrm{Ga_2O_3\,(s)} \leftrightarrow 2\,\mathrm{Ga} + 1\mathrm{Ti_2O_3\,(s)}, \tag{10}$$

$$3\,\mathrm{Ti\,(s)} + \mathrm{Ga_2O_3\,(s)} \leftrightarrow 2\,\mathrm{Ga} + 3\,\mathrm{TiO\,(s)}. \tag{11}$$

The negative free energy values in Eqs. (8)–(11) indicate that oxygen prefers to react with Ti over Ga. From this, we know that the Ti/Ga_2O_3 interface is not thermodynamically stable and that under annealing, we should expect the Ti layer to oxidize and reduce the Ga_2O_3 near the interface. This is consistent with our observation of a defective Ga_2O_3 layer with Ti incorporated, adjoining a Ti/TiO_x layer in the post-annealed samples shown in Figs. 2–6. It is perhaps surprising that the reactions proceed so rapidly, given that the post-deposition anneal duration was only 1-min. Our observation of a rapidly changing interface agrees with the observation made by Yao *et al.*[13] that the ohmic nature of a Ti/Ga_2O_3 contact deteriorated when the sample was annealed in argon at temperatures above 500 °C for 1 min. In a power device, such interfacial reactions may occur or be advanced during extended thermal or electrical bias/current stress. Similar interfacial reactions may cause unexpected changes in contact behavior for both ohmic and Schottky contacts.

The thermodynamic properties of the reactions at room temperature (298.15 K) are also calculated and shown in Table II. It is noticeable that even at room temperature, the interfacial reaction between Ti and Ga_2O_3 still favors oxidation of titanium. This suggests that the interface will gradually degrade during device operation.

In all the images, it is observed that the original 20-nm Ti layer shrank to around 5-nm thick after the 1-min 470 °C N_2 anneal. From the EDX mapping in Fig. 5, it is clear that the Ti and Au layers have significantly interdiffused. This concurs with previous work[31,32] on Ti/Au thin films which showed that Ti diffuses along the grain boundary of Au toward the free surface and with Yao *et al.*'s observation of interdiffusion in an Au/Ti/Ga_2O_3 contact after a 1-min 400 °C anneal.[12] In our samples, annealing forms an intermixed matrix of Au-Ti that is in contact with the thin Ti-TiO_x layer. We suggest that the ohmic I-V characteristics observed for annealed Ti/Ga_2O_3 contacts may be due, in large part, to the proximity of the metallic Au-Ti intermixed layer to the heavily Sn-doped Ga_2O_3 substrate.

TABLE I. Thermodynamic constants for gallium oxide and various titanium oxides at 470 °C (743 K), where the Ga entropy value is for liquid gallium and is marked with a (ℓ). A ΔS_{Oxygen} of 233.4 J/mol/K is used to calculate ΔG_f of various oxides. Values are from Refs. 20 and 30.

Compounds	ΔH_f (kJ/mol)	ΔS (J/mol/K)	ΔG_f (kJ/mol)	$\Delta H_{f,Metal}$ (kJ/mol)	ΔS_{Metal} (J/mol/K)	ΔG_{rxn} (kJ/mol)
Ga_2O_3	−1048.1	169.1	−788.7	17.59 (ℓ)	84.0 (ℓ)	...
TiO_2	−919.5	100.8	−779.4	12.38	55.9	−364
Ti_3O_5	−2390.5	270.7	−2033.4	12.38	55.9	−418
Ti_2O_3	−1477.6	167.8	−1258.9	12.38	55.9	−460
TiO	−501.9	86.5	−437.9	12.38	55.9	−527

TABLE II. Thermodynamic constants for gallium oxide and various titanium oxides at room temperature (298.15 K), where the Ga entropy value is for solid gallium and is marked with an (s). A ΔS°_{Oxygen} of 205.2 J/mol/K is used to calculate ΔG°_f of various oxides. Values are from Refs. 20 and 30.

Compounds	ΔH°_f (kJ/mol)	ΔS° (J/mol/K)	ΔG°_f (kJ/mol)	$\Delta H^\circ_{f,Metal}$ (kJ/mol)	ΔS°_{Metal} (J/mol/K)	ΔG°_{rxn} (kJ/mol)
Ga_2O_3	−1089	85	−998.3	0	40.8 (s)	...
TiO_2	−944	50.6	−888.8	0	30.7	−335
Ti_3O_5	−2459	129.3	−2317	0	30.7	−392
Ti_2O_3	−1521	78.8	−1434	0	30.7	−436
TiO	−519.7	50	−495	0	30.7	−486

Within the Au/Ti layer, about 3 nm above the Ti-TiO_x layer interface, a discontinuous Ti-rich nanocrystalline layer is observed. The dark dots in Fig. 2(a) indicate the different chemical composition of these crystallites compared to the bright background, which corresponds to gold. The lattice planes observed in STEM images [Figs. 2(a) and 2(b)] suggest that these regions are crystallites, with an average diameter of 3-5 nm. The FFT patterns of the Ti-rich nanocrystals [Fig. 3(f)] are distinct from those of the Au (111) region [Fig. 3(g)]. This suggests that the Ti-rich nanocrystals have different structures from the Au matrix. From EDX [Fig. 5(e), in the range of 14-20 nm] and EELS (Fig. 6) analyses, we verified that these dark nanocrystals are Ti-rich crystalline particles. We note that, since in this region there is a moderate amount of oxygen incorporated [Figs. 5(e) and 6(c)], these crystallites are unlikely to be an Au-Ti intermetallic compound. A more likely hypothesis is that Ti reacts with oxygen present to form TiO_x nanoparticles, which segregate from the Au-Ti intermixed matrix. In the EDX measurement, we observe a non-zero Ga tail in the Au layer, far from the Ti/Ga_2O_3 interface, i.e., at 0-24 nm in Fig. 5(e). This Ga tail may be due to FIB sample preparation using a Ga ion beam or due to EDX measurement artifacts.

Based on this study, the good electrical contact between Ti/Au metallization and Sn-doped β-Ga_2O_3 can be tentatively attributed to the following causes. First, the formation of a thin Ti-TiO_x layer between the metal (Au/Ti) layer and the β-Ga_2O_3 layer may provide a relatively efficient pathway for electron transport. It is suspected that the relatively small bandgap of TiO_x compared to Ga_2O_3 (e.g., ~3.2 eV for rutile TiO_2)[33] and the thinness of the layer facilitates the transport of electrons through the Ti-TiO_x layer. Second, lattice matching of the defective β-Ga_2O_3 layer and part of the Ti-TiO_x layer to β-Ga_2O_3 may lower the collision probability of electrons passing through the contact, enhancing the carrier mobility and thus reducing contact resistivity. Finally, the interdiffusion of Au and Ti may narrow the distance between the low-resistance Au layer and heavily doped β-Ga_2O_3. In addition, the diffusion of Sn or its interactions with other elements may facilitate the formation of the ohmic contact. In the present study, we did not attempt to definitively identify the roles of Sn nor of the observed Ti-rich nanocrystals, in ohmic conduction.

Sn-doped β-Ga_2O_3 has been frequently used for electronic devices and is known to form ohmic contacts readily to Ti/Au electrode layers. However, the physical mechanisms for contact formation have never been fully explained, and the Ti/β-Ga_2O_3 interface is not predicted to be thermodynamically stable at elevated temperatures. Here we show that, after a standard ohmic annealing (470 °C 1 min in N_2), elemental diffusion and reactions occur at the Ti/β-Ga_2O_3 interface which may be responsible for the good ohmic behavior. The formation of a thin Ti-TiO_x layer partially lattice matched to β-Ga_2O_3 and Au diffusion toward the contact interface are the two most likely contributors to ohmic behavior. Further work needs to be performed to understand the role of the Ti-rich nanocrystal layer, observed here, in electrical conduction. In addition, future work can address the various roles that Sn or other impurities and crystal orientation may play in the thermodynamic evolution of the interfaces and their electrical properties and assess whether similar interfacial reactions occur in more complex ohmic electrode stacks (e.g., Ti/Al/Ni/Au) or Schottky contacts.

This work was supported by the Department of the Navy, Office of Naval Research under ONR Award No. N00014-17-1-2998 with Dr. Paul Maki. Any opinions, findings, and conclusions or recommendations expressed in this material are those of the author(s) and do not necessarily reflect the views of the Office of Naval Research. Portions of this work were conducted in Lurie Nanofabrication Facility (LNF) and Michigan Center for Materials Characterization (MC)^2, which are supported by the University of Michigan College of Engineering. The authors thank Kai Sun for advice on STEM/TEM measurements and Zumrad Kabilova for mask design. The FEI Nova 200 Nanolab, JEOL 2010F AEM and JEOL 2100F AEM instruments were funded by NSF Award Nos. DMR-0320740, DMR-9871177, and DMR-0723032, respectively.

REFERENCES

[1] A. J. Green, K. D. Chabak, E. R. Heller, R. C. Fitch, M. Baldini, A. Fiedler, K. Irmscher, G. Wagner, Z. Galazka, S. E. Tetlak, A. Crespo, K. Leedy, and G. H. Jessen, IEEE Electron Device Lett. **37**, 902 (2016).
[2] K. Konishi, K. Goto, H. Murakami, Y. Kumagai, A. Kuramata, S. Yamakoshi, and M. Higashiwaki, Appl. Phys. Lett. **110**, 103506 (2017).
[3] X. Yan, I. S. Esqueda, J. Ma, J. Tice, and H. Wang, Appl. Phys. Lett. **112**, 032101 (2018).
[4] S. Fujita, Jpn. J. Appl. Phys., Part 1 **54**, 030101 (2015).
[5] M. Higashiwaki, K. Sasaki, H. Murakami, Y. Kumagai, A. Koukitu, A. Kuramata, T. Masui, and S. Yamakoshi, Semicond. Sci. Technol. **31**, 034001 (2016).
[6] S. J. Pearton, J. Yang, P. H. Cary, F. Ren, J. Kim, M. J. Tadjer, and M. A. Mastro, Appl. Phys. Rev. **5**, 011301 (2018).

[7]T. Onuma, S. Saito, K. Sasaki, T. Masui, T. Yamaguchi, T. Honda, and M. Higashiwaki, Jpn. J. Appl. Phys., Part 1 **54**, 112601 (2015).
[8]N. Ueda, H. Hosono, R. Waseda, and H. Kawazoe, Appl. Phys. Lett. **70**, 3561 (1997).
[9]Z. Galazka, K. Irmscher, R. Uecker, R. Bertram, M. Pietsch, A. Kwasniewski, M. Naumann, T. Schulz, R. Schewski, D. Klimm, and M. Bickermann, J. Cryst. Growth **404**, 184 (2014).
[10]T. Oishi, Y. Koga, K. Harada, and M. Kasu, Appl. Phys. Express **8**, 031101 (2015).
[11]K. Zeng, A. Vaidya, and U. Singisetti, IEEE Electron Device Lett. **39**, 1385 (2018).
[12]M. Higashiwaki, K. Sasaki, T. Kamimura, M. Hoi Wong, D. Krishnamurthy, A. Kuramata, T. Masui, and S. Yamakoshi, Appl. Phys. Lett. **103**, 123511 (2013).
[13]Y. Yao, R. F. Davis, and L. M. Porter, J. Electron. Mater. **46**, 2053 (2017).
[14]M. Higashiwaki, K. Sasaki, A. Kuramata, T. Masui, and S. Yamakoshi, Appl. Phys. Lett. **100**, 013504 (2012).
[15]K. Zeng, J. S. Wallace, C. Heimburger, K. Sasaki, A. Kuramata, T. Masui, J. A. Gardella, and U. Singisetti, IEEE Electron Device Lett. **38**, 513 (2017).
[16]M. H. Wong, K. Sasaki, A. Kuramata, S. Yamakoshi, and M. Higashiwaki, IEEE Electron Device Lett. **37**, 212 (2016).
[17]K. Sasaki, M. Higashiwaki, A. Kuramata, T. Masui, and S. Yamakoshi, Appl. Phys. Express **6**, 086502 (2013).
[18]D. K. Schroder, *Semiconductor Material and Device Characterization*, 3rd ed. (John Wiley & Sons, Inc., Hoboken, NJ, 2015).
[19]M. Ahmad and B. M. Arora, Solid-State Electron. **35**, 1441 (1992).
[20]W. M. Haynes, *CRC Handbook of Chemistry and Physics*, 96th ed. (CRC Press, 2015).
[21]S. Manandhar and C. V. Ramana, Appl. Phys. Lett. **110**, 061902 (2017).
[22]Y. Tomm, J. M. Ko, A. Yoshikawa, and T. Fukuda, Sol. Energy Mater. Sol. Cells **66**, 369 (2001).
[23]L. Binet, D. Gourier, and C. Minot, J. Solid State Chem. **113**, 420 (1994).
[24]C. Tang, J. Sun, N. Lin, Z. Jia, W. Mu, X. Tao, and X. Zhao, RSC Adv. **6**, 78322 (2016).
[25]J. B. Varley, J. R. Weber, A. Janotti, and C. G. Van de Walle, Appl. Phys. Lett. **97**, 142106 (2010).
[26]V. Wang, W. Xiao, L.-J. Kang, R.-J. Liu, H. Mizuseki, and Y. Kawazoe, J. Phys. Appl. Phys. **48**, 015101 (2015).
[27]E. Korhonen, F. Tuomisto, D. Gogova, G. Wagner, M. Baldini, Z. Galazka, R. Schewski, and M. Albrecht, Appl. Phys. Lett. **106**, 242103 (2015).
[28]J. B. Varley, H. Peelaers, A. Janotti, and C. G. Van de Walle, J. Phys.: Condens. Matter **23**, 334212 (2011).
[29]B. E. Kananen, L. E. Halliburton, K. T. Stevens, G. K. Foundos, and N. C. Giles, Appl. Phys. Lett. **110**, 202104 (2017).
[30]M. W. Chase and National Institute of Standards and Technology (U.S.), NIST-JANAF *Thermochemical Tables*, 4th ed. (American Chemical Society and American Institute of Physics for the National Institute of Standards and Technology, 1998).
[31]W. E. Martinez, G. Gregori, and T. Mates, Thin Solid Films **518**, 2585 (2010).
[32]T. C. Tisone and J. Drobek, J. Vac. Sci. Technol. **9**, 271 (1972).
[33]M. M. Abdel-Aziz, I. S. Yahia, L. A. Wahab, M. Fadel, and M. A. Afifi, Appl. Surf. Sci. **252**, 8163 (2006).